

Hybrid organic-inorganic nanotubes effectively adsorb some organic pollutants in aqueous phase

Original

Hybrid organic-inorganic nanotubes effectively adsorb some organic pollutants in aqueous phase / Nasi, R.; Sannino, F.; Picot, P.; Thill, A.; Oliviero, O.; Esposito, S.; Armandi, M.; Bonelli, B.. - In: APPLIED CLAY SCIENCE. - ISSN 0169-1317. - 186:(2020), p. 105449. [10.1016/j.clay.2020.105449]

Availability:

This version is available at: 11583/2801715 since: 2022-09-22T15:46:42Z

Publisher:

Elsevier Ltd

Published

DOI:10.1016/j.clay.2020.105449

Terms of use:

This article is made available under terms and conditions as specified in the corresponding bibliographic description in the repository

Publisher copyright

Elsevier postprint/Author's Accepted Manuscript

© 2020. This manuscript version is made available under the CC-BY-NC-ND 4.0 license
<http://creativecommons.org/licenses/by-nc-nd/4.0/>. The final authenticated version is available online at:
<http://dx.doi.org/10.1016/j.clay.2020.105449>

(Article begins on next page)

27
28
29
30
31
32
33
34
35
36
37
38
39
40
41
42
43
44
45
46
47
48
49
50
51
52

Abstract

Methylimogolite nanotubes (Me-IMO NTs, chemical composition $(\text{OH})_3\text{Al}_2\text{O}_3\text{SiCH}_3$) are characterized by having an inner hydrophobic (fully-methylated) surface. Conversely, the outer surface is hydrophilic and positively charged below the point of zero charge (at $\text{pH} = 8.6$), due to the $\text{Al}(\text{OH})\text{Al} + \text{H}^+ = \text{Al}(\text{OH})_2^+\text{Al}$ equilibrium occurring at the outer surface of the NTs when they are dispersed in water.

In this work, adsorption of MCPA (2-methyl-4-chlorophenoxyacetic acid) and of dichloromethane (DCM) on Me-IMO NTs was studied by means of both adsorption/desorption measurements in batch conditions (at room temperature and at different pH value) and Small Angle X-rays Scattering (SAXS).

MCPA, which partially dissociates in water ($\text{pK}_a = 2.90$), is mainly adsorbed at the outer surface of the NTs, although measurements in batch conditions show that other types of interaction occur (i.e. H-bond) at higher MCPA concentration. SAXS measurements confirm that MCPA has not entered the NTs inner pores.

Interaction of the NTs with DCM, instead, is more complex: SAXS measurements show that DCM molecules interact with the NTs inner surface, whereas batch experiments indicate that additional interactions take place with the outer surface of the NTs.

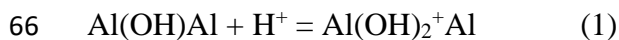
53

54 **Introduction**

55 Hybrid organic-inorganic nanotubes (NTs) with chemical formula $(\text{OH})_3\text{Al}_2\text{O}_3\text{SiCH}_3$ (Me-
56 IMO) can be synthesized in water by a template-free sol-gel procedure, starting from commercial
57 precursors, i.e. an Al salt (or alkoxide) and triethoxymethylsilane (TEMS) (Bottero et al., 2011). Dual
58 functionalization of the inner surface is also possible to a certain extent (Picot et al., 2019) and Ge-
59 analogues can be obtained, as well (Amara et al., 2015).

60 Me-IMO NTs have unique properties: they are mainly mesoporous with remarkably high
61 accessible specific surface area (about $650 \text{ m}^2 \text{ g}^{-1}$) and are thermally stable up to $300 \text{ }^\circ\text{C}$ (Mackenzie,
62 1989; Bottero et al., 2011). When dispersed in water, the NTs are positively charged at pH values
63 below 9 (Bahadori et al., 2018). Such positive charge stems, in part, from the acid-base properties of
64 external -OH groups (Gustafsson, 2001) as in eq. (1):

65



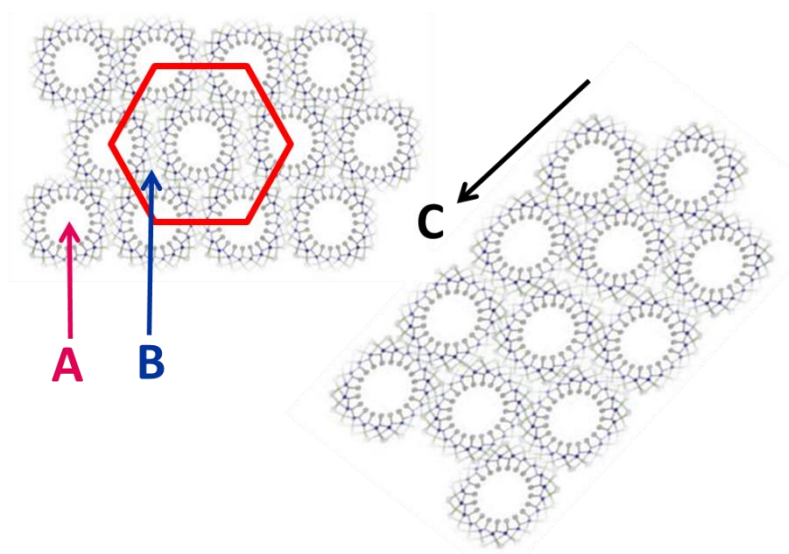
67

68 and, in part, from some curvature effects (Poli et al., 2015).

69 Proper (inorganic) imogolite (IMO) NTs (Cradwick et al., 1972), which can be obtained by
70 sol-gel methods as well (Du et al., 2017), have different structure (Thill et al., 2017) and applications,
71 depending on whether they occur as a powder or in aqueous suspension of freshly synthesized NTs.
72 Aqueous dispersions of pristine IMO NTs, which have never been dried, do not show any bundles,
73 since the NTs repel each other, due to their positive surface charge. The NTs may form bundles upon
74 addition of salt or upon increase of pH. In such a case, bundles formation is irreversible to a large
75 extent (Karube, 1998).

76 Surprisingly, even in freshly synthesized dispersions, Me-IMO NTs are always observed to
77 form bundles (Scheme 1), where three types of pores A, B and C can be identified (Ackerman et al.,
78 1993). Noticeably, in Me-IMO the A pores have an average diameter of 2.0 nm and are extremely

79 hydrophobic, whereas in IMO they have an average diameter of 1.0 nm and are extremely hydrophilic
80 (Bonelli et al., 2009; Zanzottera et al., 2012b); the B pores are 0.45 nm wide in Me-IMO, allowing
81 adsorption of small probes in gas/solid systems (Zanzottera et al., 2012a; Bonelli et al., 2013a), being
82 instead smaller in IMO (*ca.* 0.30 nm) and, thus, less accessible to gas probes (Ackerman et al., 1993).
83 Finally, the C pores (Scheme 1) are larger slit-mesopores, accessible to large molecules (Garrone and
84 Bonelli, 2016; Shafia et al., 2016a) and characterized by amphoteric properties (Bonelli et al., 2009,
85 2013b) in both Me-IMO and IMO.



86

87

Scheme 1.

88

Three types of pores occurring in Me-IMO NTs in the powder form.

89

90 Although also gels may be obtained, usually powders of Me-IMO NTs are obtained (Bottero
91 et al., 2011). In water, the positively charged outer surface (eq. 1) favours both NTs re-dispersion,
92 and interaction with negatively charged species (Bonelli, 2016) and/or polar molecules (Boyer et al.,
93 2014). Nonetheless, some of us showed that in oil-in-water emulsion, Me-IMO NTs adsorb at the
94 oil/water interface, stabilizing the emulsion by inducing slow oil-triggered modifications of the viscosity
95 of the continuous phase and, possibly, favouring transport of small molecules within the NTs (Picot et al.,
96 2016).

97 With Me-IMO NTs, the simultaneous occurrence of an inner hydrophobic surface and an outer
 98 hydrophilic (and positively charged surface) may be of interest in applications implying selective
 99 adsorption, like gas membranes, adsorption of complex mixtures and removal of water pollutants, as
 100 well. Indeed, IMO has been proposed as an optimal adsorbent of anions and, in particular, for
 101 phosphate fixation at the outer surface of the NTs (Mizota, 1977; Parfitt, 2009; Rojas-Mancilla et al.,
 102 2019).

103 There is currently a great interest into the development of new nanomaterials able to
 104 efficiently remove from water several organic pollutants, besides inorganic ones, like agrochemicals,
 105 dyes, halogenated compounds, pharmaceutical and personal care products, etc. (Freyria et al., 2018).
 106 Some of us studied the adsorption and degradation of the azo-dye Acid Orange 7 (AO7,
 107 $C_{16}H_{11}N_2SO_4Na$) in the presence of aqueous suspensions of IMO, Me-IMO or Fe^{3+} -doped NTs
 108 (Shafia et al., 2016a; Bahadori et al., 2018). Some interesting insights were obtained, like the
 109 preferential interaction of AO7 moieties (negatively charged in water) with the outer surface of NTs,
 110 although some of the inner Si-OH groups of IMO NTs (likely those at the mouth of A pores) were
 111 able to interact with the pollutant by H-bonding. In the presence of Fe^{3+} species, instead, a ligand
 112 displacement phenomenon was observed, where Fe^{3+} ions were able to coordinate the dye through its
 113 N atoms. (Shafia et al., 2016a). This work focuses, instead, on the interaction of Me-IMO NTs with
 114 two organic molecules (Table 1) in water suspension, namely 4-chloro-2-methylphenoxyacetic acid
 115 (MCPA) and dichloromethane (DCM).

116

117 **Table 1**

118 Some properties of MCPA and DCM.

Pollutant	Molecule dimension(s) (nm)	Dipole Moment (D)	pKa	Solubility in water (g/L)	Bulk Electron density ($e/\text{\AA}^3$)
MCPA	~ 0.8 x 0.7		2.90	0.825 at 23 °C ^b	0.480
DCM	0.33 ^a	1.470	-	17.5 at 25 °C	0.396

119 ^aKinetic diameter

120 ^b(Gimeno et al., 2003)

121

122 MCPA is a phenoxy herbicide extensively used in agriculture to control annual and perennial
123 weeds in cereals, grasslands, trees and turf: being highly soluble in water and very mobile, it can
124 leach from soil and can be found in groundwater wells, thus posing serious environmental problems.
125 For this reason, the U.S. Environmental Protection Agency (EPA) classifies MCPA as a potential
126 groundwater contaminant (Addorisio et al., 2010).

127 DCM is a chlorinated volatile organic compound (VOC), which is soluble in water due to its
128 dipole moment ($\mu_{\text{DCM}} = 1.470 \text{ D}$): it is mainly used as solvent and reagent, being also employed in the
129 manufacture of aerosols, adhesives, and for dry cleaning (Huang et al., 2014). In addition to its high
130 toxicity and carcinogenic character, DCM contributes to global warming, depletion of the ozone
131 layer, and photochemical smog: the U.S. EPA has included it among the 17 highly dangerous
132 chemicals that should be targeted for emissions reduction.

133 In this work, a sample of Me-IMO NTs was characterized by powder X-ray Diffraction
134 (XRD), N_2 isotherms at $-196 \text{ }^\circ\text{C}$, ζ -potential measurements and SAXS and was tested as adsorbent of
135 either MCPA or DCM by means of adsorption/desorption experiments in batch conditions and by
136 SAXS.

137

138 **2. Materials and Methods**

139 *2.1 Me-IMO synthesis*

140 A sample of Me-IMO was synthesized according to a procedure reported elsewhere (Bottero
141 et al., 2011). In acidic medium due to HClO_4 , Al-*sec*-butoxide (ASB) and triethoxymethylsilane
142 (TEMS) were used as the Al and Si source, respectively, with molar ratio Al : Si = 2 : 1.15. The slight
143 excess of TEMS was used to prevent formation of by-products (i.e. Al hydroxide) due to fast
144 hydrolysis of ASB, which is a crucial issue in the synthesis. For the same reason, the sample was
145 synthesised in a dry room (i.e. a moisture-free environment) (Shafia et al., 2016b).

146

147 *2.2. Me-IMO characterization*

148 X-ray powder diffraction (XRD) were measured in the 2.5–20° 2 θ range on an 'Xpert
149 Diffractometer (Cu K α radiation; λ =1.5414 Å, step width = 0.02 2 θ).

150 The values of BET SSA (Brunauer Emmett Teller Specific Surface Area), total pore volume
151 and *t*-plot microporous volume reported in Table 2 were calculated from the N₂ adsorption/desorption
152 isotherm measured at -196 °C on the powder outgassed at 275 °C in order to remove residual water
153 and atmospheric contaminants. The Non Local-Density Function Theory Pore Size Distribution (NL-
154 DFT PSD) and the corresponding cumulative pore volume curve were obtained by applying a N₂-
155 silica kernel (for cylindrical pores) to the isotherm adsorption branch.

156 The Al/Si ratio was measured by means of Energy Dispersive X-ray analysis (EDX, AZTec,
157 Oxford Instruments) on three different spots (ca. 0.1 mm² area each): the so-obtained average value
158 Al/Si = 0.49 was in fair agreement with the theoretical one Al/Si = 0.50.

159 Electrophoretic mobility as a function of pH was measured at 25°C by means of light
160 scattering technique on a Zetasizer Nano-ZS instrument (Malvern Instruments, Worcestershire, UK).
161 The corresponding ζ -potential curve was calculated according to the Henry's equation $UE =$
162 $2\epsilon\zeta f(Ka)/3\eta$, where UE is the electrophoretic mobility, ϵ is the dielectric constant, ζ is the zeta
163 potential, $f(Ka)$ is the Henry's function, and η is the viscosity. The adopted value of $f(Ka)$ was 1.5, in
164 agreement with the Smoluchowski approximation, usually applied to aqueous solutions of moderate
165 electrolyte concentration, as in the present case. Water suspensions were obtained after 2 min
166 sonication with an ultrasonic probe (100 W, 20 kHz, Sonoplus; Bandelin, Berlin, Germany); the pH
167 of the suspension was then adjusted by adding either 0.10 M HCl or 0.10 M NaOH.

168 SAXS (Small Angle X-ray Scattering) data were acquired on a Xeuss 2.0 HR SAXS/WAXS
169 instrument (Xenocs) equipped with a microfocus Copper sealed tube (30 W/30 μ m) ; single reflection
170 multilayer optic with 2D collimation for Cu K α (λ =1.5414 Å) and 2 motorized scatter-less slits 2.0
171 with variable aperture enable the definition of the beam energy (Cu K α with spectral purity > 97 %)
172 and size while minimizing the scattering background. The divergence of the beam is < 0.4 mrad in

173 both planes perpendicular to beam axis. The sample were measure in the high resolution beam
174 configuration with a max flux at the sample position of 1×10^8 (ph/s).

175 Me-IMO NTs were studied both as powder and in water suspension: in the former case, the
176 powder was fixed between two Kapton films and placed in aluminium frame (Fig. 6), whilst glass
177 capillaries containing dispersion and contaminants were vacuum tight sealed and placed in a different
178 aluminium sample holder that can accommodate up to 20 capillaries.

179 MCPA adsorption on MeIMO has been evaluated by SAXS, as follows: a stock dispersion of
180 5g/L of MeIMO in 100 μ M of herbicide water (MilliQ) solution was prepared (natural pH 4.45). From
181 the stock MeIMO dispersion three samples were also prepared at different pH (3, 4.45, 9.65, 10.46)
182 by means of HCl or NH₃ addition.

183 DCM adsorption on Me-IMO has been evaluated by SAXS at natural pH.

184

185 *2.3 Adsorption/desorption experiment in batch-conditions*

186 4-chloro-2-methylphenoxyacetic acid (MCPA) and Dichloromethane (DCM) were purchased
187 from Sigma-Aldrich Chemical Co. (Poole, Dorset, U.K.; 99.0% purity). HPLC grade solvents (Carlo
188 Erba, Milan, Italy) were used without further purification. All the other chemicals were from Sigma-
189 Aldrich, unless otherwise specified.

190 For MCPA experiments, a stock solution of the herbicide was prepared by dissolving 200 mg
191 MCPA in 1000 mL of ultrapure water (final concentration 1000 μ mol L⁻¹) and, then, kept refrigerated.

192 For DCM experiments, a stock solution of the organic pollutant was prepared by diluting
193 DCM with ultrapure water (final concentration 0.15 mol L⁻¹).

194

195 *2.3.1 Analytical determination of the organic contaminants*

196 The concentration of MCPA was measured on an Agilent 1200 Series HPLC apparatus
197 (Wilmington, DE), equipped with a DAD array and a ChemStation Agilent Software. A Macharey-
198 Nagel Nucleosil 100-5 C18 column (stainless steel 250 4 mm) was used.

199 For MCPA determination, the mobile phase, comprising a binary system of 50:50 acetonitrile:
200 phosphate buffer (0.1%, pH 2.5), was pumped at 1 mL min⁻¹ flow in isocratic mode. The UV detector
201 was set at 225 nm. The quantitative determination of MCPA was performed by elaborating its
202 corresponding calibration curve in the 0.25 - 1000 µmol L⁻¹ range.

203 The concentration of DCM was determined by Gas Chromatography-Mass Spectrometry
204 (GC-MS). The samples were analysed on a Perkin-Elmer AutoSystemTMXL GC, equipped with a
205 Programmed-Temperature Split/Splitless injector with programmable pneumatic control kept at a
206 constant temperature of 250 °C; a Restek Rtx-5MS capillary column (5% diphenyl-95%
207 dimethylpolysiloxane, 30 m x 0.25 mm, 0.25 µm) and a Perkin-Elmer Turbo Mass Goldmass-
208 spectrometer. The oven temperature was programmed to run at 60 °C for 5 min and then to increase
209 by 15 °C min⁻¹ to a final temperature of 280 °C. A NIST mass spectral library version 1.7 was used
210 for peak identification. The quantitative determination of DCM was performed elaborating its
211 corresponding calibration curve in the 0.0125 and 0.15 mol L⁻¹ range.

212

213 *2.3.2 Study of the effect of pH, time and concentration of MCPA*

214 To evaluate the effect of pH, MCPA sorption experiments were carried out at solid/liquid ratio
215 of 0.5 g L⁻¹ obtained by adding 5 mg of NTs to a final volume of 10 mL, using a fixed pesticide
216 concentration of 10 µmol L⁻¹, obtained by diluting 1000 µmol L⁻¹ stock solution, varying the pH from
217 3.0 to 9.5 and for an incubation time of 24 h. The pH was controlled by addition of 0.01 mmol L⁻¹
218 HCl or NaOH to the solution. After incubation in a rotatory shaker at 20 °C, the samples were
219 centrifuged at 7000 rpm for 20 min. The amount of adsorbed MCPA was calculated as the difference
220 between the MCPA quantity initially added and that present in the liquid at equilibrium. Blanks of
221 MCPA in ultrapure water were analyzed in order to check for pesticide stability and/or sorption on
222 the vials.

223 To evaluate the effect of time on MCPA adsorption, experiments were performed at
224 solid/liquid ratio of 0.5 g L⁻¹ using 7.0 µmol L⁻¹ of MCPA at pH 3.5. The suspensions were stirred

225 for 2.0, 5.0, 10, 20, 40, 60, 90, 120, 300, 1080, 1440, 1680 and 2880 min. Different volumes of a
226 stock solution of herbicide ($1000 \mu\text{mol L}^{-1}$) were added to the NTs containing liquid to have initial
227 MCPA concentration in the $0.05 - 260 \mu\text{mol L}^{-1}$ range. The pH was kept constant at 3.5 by addition
228 of 0.10 or 0.01 mol L^{-1} HCl or NaOH. The samples were incubated for 1440 min and, then, after
229 centrifugation, the supernatants were analyzed as described above.

230 During desorption experiments, immediately after adsorption of 255 and $170 \mu\text{mol L}^{-1}$ initial
231 MCPA concentration, the samples were put in contact with different volumes of ultrapure water, so
232 to determine the amount of released herbicide. In particular, 10 mL of supernatant was removed and
233 replaced with 10 mL of ultrapure water. After shaking at $25 \text{ }^\circ\text{C}$ for 24 h , the suspensions were
234 centrifuged and the concentration of released herbicide in the supernatant was determined. The same
235 procedure was repeated by replacing 3.0 , 4.0 , and 6.0 mL of supernatant with the same volume of
236 ultrapure water.

237 238 *2.3.3 Study of the effect of pH, time and concentration of DCM*

239 In order to study the effect of pH, sorption experiments were made at a solid/liquid ratio of
240 0.5 g L^{-1} obtained by adding 5 mg solid to a final volume of 10 mL , using a constant DCM
241 concentration of 0.15 mol L^{-1} , varying the pH from 3.5 to 7.0 and with an incubation time of 24 h .
242 pH was controlled by addition of 0.01 mmol L^{-1} HCl or NaOH. After incubation in a rotatory shaker
243 at $20 \text{ }^\circ\text{C}$, the samples were centrifuged at 7000 rpm for 20 min . The amount of adsorbed DCM was
244 calculated as the difference between the initially added quantity of DCM and the quantity present at
245 equilibrium in the liquid. Blanks of DCM in ultrapure water were analysed in order to check for
246 pollutant stability and sorption on the vials.

247 In order to study the effect of time, experiments were performed at a solid/liquid ratio of 0.5
248 g L^{-1} by using 0.15 mol L^{-1} of DCM at pH 5.5 . The suspensions were stirred for 2.0 , 5.0 , 10 , 20 , 40 ,
249 60 , 90 , 120 , 300 , 1080 , 1440 , 1680 and 2880 min .

250 The adsorption isotherm was obtained as follows: different volumes of a stock solution of
251 DCM (0.15 mol L^{-1}) were added to the Me-IMO NTs containing liquid in such a way to have an
252 initial DCM concentration in the $0.0125 - 0.15 \text{ mol L}^{-1}$ range. The pH of each suspension was kept
253 constant at 5.5 by adding 0.10 or 0.01 mol L^{-1} HCl or NaOH. The samples were incubated for 300
254 min and, then, after centrifugation, the supernatants were analysed as described above.

255 During desorption experiments, the sample obtained immediately after adsorption from 0.15
256 mol L^{-1} DCM initial concentration, was put in contact with different volumes of ultrapure water at
257 standard pH value, so to determine the amount of released DCM. In particular, 10 mL of supernatant
258 was removed and replaced by 10 mL of ultrapure water. After shaking at $25 \text{ }^\circ\text{C}$ for 5 h, the suspension
259 was centrifuged and the concentration of released DCM was determined. The same procedure was
260 made by replacing 3.0, 4.0, and 6 mL of supernatant with the same volume of ultrapure water.

261

262 **3. Results and discussion**

263 *3.1. Relevant physico-chemical features of the Me-IMO NTs in powder and water suspension.*

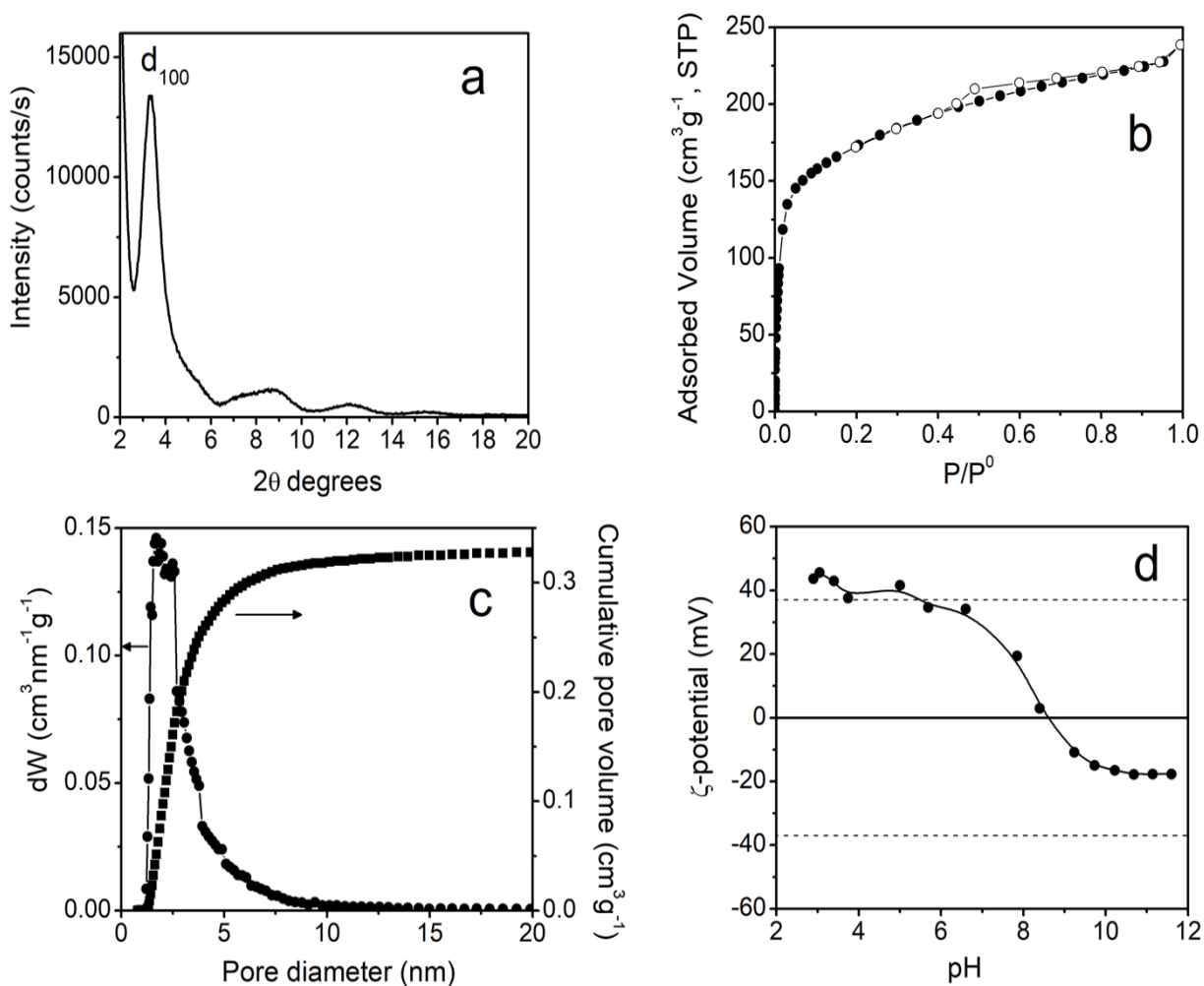
264 Figure 1 reports the powder XRD pattern (a), the N_2 adsorption/desorption isotherm at -196
265 $^\circ\text{C}$ (b), the PSD and cumulative volume (c) and the ζ -potential curve (d) of the Me-IMO NTs. In Fig.
266 1a, the main reflection at $3.32 \text{ } 2\theta$ and the halo at $8.84 \text{ } 2\theta$ degrees are characteristic of NTs organized
267 into a pseudo-hexagonal arrangement (Bursill et al., 2000; Bottero et al., 2011). The value of the cell
268 parameter (Table 2) was $a = 3.02 \text{ nm}$, as calculated by applying the equation $a = \frac{2}{\sqrt{3}} d_{100}$: the cell
269 parameter is larger than that of IMO NTs (Cradwick et al., 1972), due to larger A pores (*vide infra*).

270 Fig. 1b shows a type IV N_2 isotherm, with a limited (type H4) hysteresis loop. The steep
271 increase of the adsorbed volume at low P/P^0 values indicates occurrence of some micropores, whereas
272 the rounded knee below $0.1 P/P^0$ is due to the presence of very narrow mesopores. The corresponding
273 values of BET SSA and pore volume (Table 2) are typical of Me-IMO NTs (Bottero et al., 2011).
274 Accordingly, the PSD curve (circles in Fig. 1c) shows the occurrence of (mainly) narrow mesopores

275 with an average diameter of *ca.* 2.0 nm (A pores). The value of micropore volume that can be
 276 extrapolated from the cumulative pore volume curve (squares in Fig. 1c) is close to that reported in
 277 Table 2, which is obtained by the *t*-plot method ($0.085 \text{ cm}^3 \text{ g}^{-1}$).

278 The ζ -potential curve (Fig. 1d) shows that the NTs are positively charged in a broad pH range,
 279 and have a point of zero charge equal to 8.6. Nonetheless, the lines at $\zeta = \pm 37 \text{ mV}$ show range of ζ
 280 potential reported in the literature for stable suspensions (Honary and Zahir, 2013), indicating that
 281 above $\text{pH} = 5$ some NTs aggregation may occur. Such a phenomenon could affect the
 282 adsorption/desorption experiments (*vide infra*).

283



284

285 **Figure 1.** Section a: low angle XRD pattern of Me-IMO powder; section b: N₂ isotherm at -
 286 196 °C (black symbols: adsorption branch; white symbols: desorption branch); section c: NL-DFT

287 PSD (circles) and cumulative pore volume (squares) as obtained by applying a N₂ - silica kernel to
 288 the isotherm adsorption branch; section d: ζ -potential curve of Me-IMO NTs as a function of pH.
 289

290 **Table 2.** Some textural properties of Me-IMO NTs as obtained by N₂ isotherms at -196 °C,
 291 X-ray powder diffraction and SAXS experiments with either the dry powder or the water dispersed
 292 one.

Sample	BET SSA (m ² g ⁻¹)	Total Pore Volume (cm ³ g ⁻¹)	<i>t</i> -plot Micropore Volume (cm ³ g ⁻¹)	Cell parameter <i>a</i> (nm) XRD	Inner radius (nm) (SAXS)	Wall thickness (nm) SAXS
Me-IMO	615	0.35	0.085	3.02	0.91 (0.92 ^a)	0.55 (0.56 ^a)

293 ^a Value for Me-IMO NTs re-suspended in water.

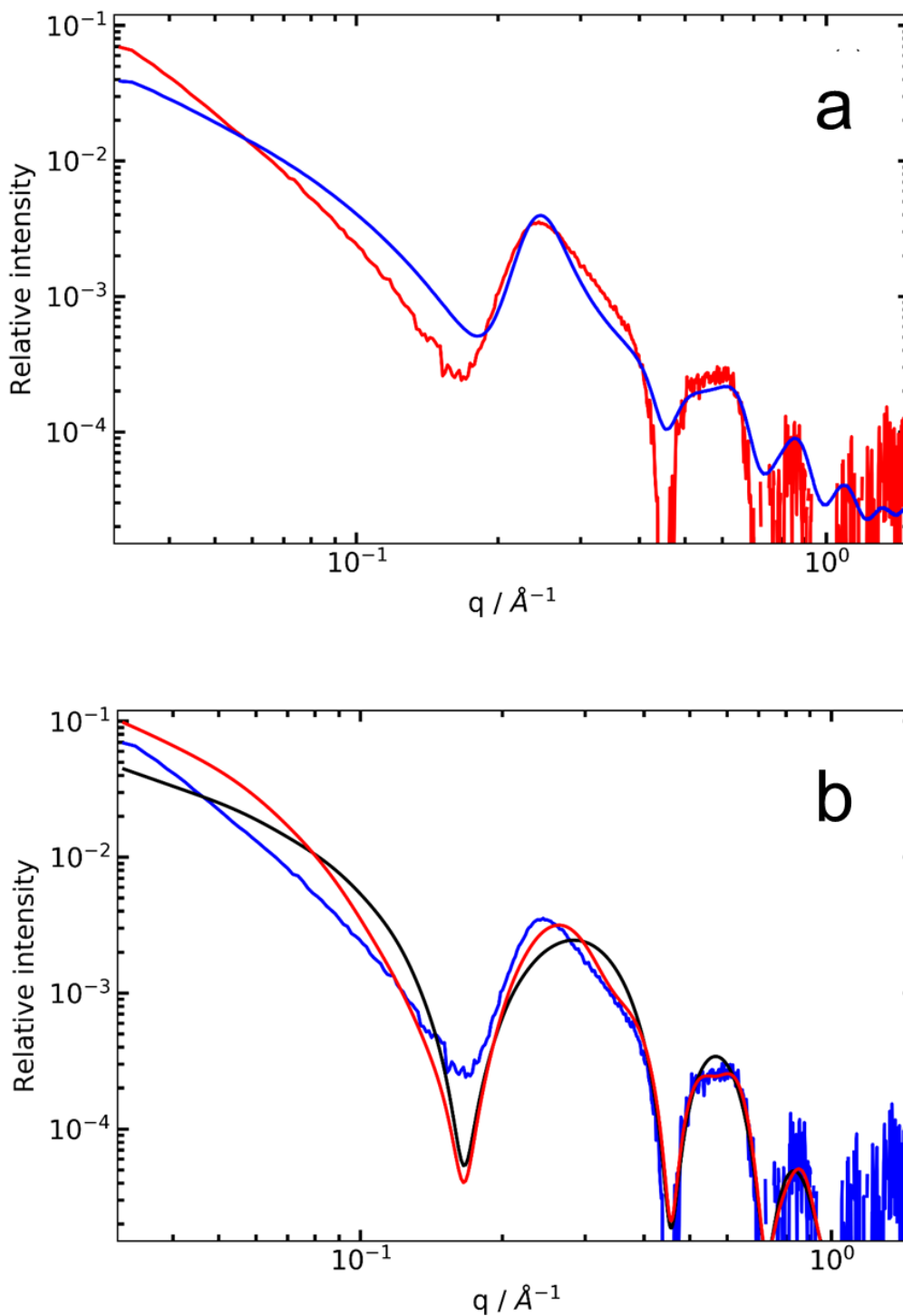
294

295 Figure 2a compares the SAXS spectra of the Me-IMO NTs powder under vacuum and of the
 296 same re-dispersed in water (NTs concentration = 5 g L⁻¹): the two patterns are very close, indicating
 297 that re-dispersion in water does not induce significant changes in the NTs shape. Only small variations
 298 at small angles indicate that the NTs bundling may be slightly affected by re-dispersion in water, with
 299 a consequent decrease of the average bundle size. The internal contrast is also modified.

300 Fig. 2b compares the experimental SAXS pattern of Me-IMO NTs powder dispersed in water
 301 (NTs concentration = 5 g L⁻¹) with the calculated patterns for isolated NTs and for NTs in small
 302 bundles. In agreement with the powder XRD pattern, comparison of the SAXS curves clearly
 303 indicates the presence of bundles when the powder is re-dispersed in water. The NTs inner radius, as
 304 obtained by SAXS, is $r_i = 0.91$ nm and the wall thickness is $t_w = 0.55$ nm. The experimental peak
 305 position in SAXS at $q = 0.238$ Å⁻¹ cannot be directly associated to the hexagonal lattice parameter
 306 due to the peak shift induced by the NTs form factor. The lattice parameter that is obtained by the
 307 computed SAXS pattern is 3.05 nm, i.e. a value that well corresponds to the NTs external diameter,
 308 with a small additional separation of 0.15 nm.

309 The geometric values obtained from XRD and SAXS are in very good agreement with the
310 pores diameter as measured by N₂ isotherm. Indeed, according to the determined sizes, the micropore
311 volume is 0.095 cm³ g⁻¹, in fair agreement with the value as determined by the *t*-plot method (0.085
312 cm³ g⁻¹). The small difference may be due to tiny amounts of water or anions trapped within the B
313 pores, which occupy a small part of the volume, finally explaining the 0.15 nm additional distance in
314 the bundle lattice parameter.

315



316

317

318

319

320

321

Figure 2. Section a: SAXS patterns of Me-IMO NTs as dry powder (blue curve) and re-
dispersed in water (5 g L⁻¹, red curve). Section b: SAXS pattern of NTs in water (blue curve)
compared to a scattering model of dispersed hollow NTs (with $r_1 = 0.91$ nm, wall thickness = 0.55
nm, internal electronic density = $0.05 \text{ e}^-/\text{\AA}^3$, black curve) and to a scattering model considering
bundles (red curve).

322

323 The SAXS analysis also allowed obtaining the inner and outer electron density (ρ_i and ρ_e) of
324 the NTs in both the dry powder and after re-dispersion in water. Interestingly, ρ_i is equal to 0.05 e^-
325 $/\text{\AA}^3$ in both samples. As compared to the electron density of bulk water ($\rho_{\text{H}_2\text{O}} = 0.334 \text{ e}^-/\text{\AA}^3$), such a
326 low inner density means that in the powder (which was treated under vacuum at r.t. and not outgassed
327 at high temperature) only few H_2O molecules occur within the NTs and that the powder is extremely
328 hydrophobic, as ρ_i did not increase upon contact with water.

329

330 3.2. Adsorption of MCPA as studied in batch conditions and by SAXS

331 Fig. 3a shows the adsorbed amount of MCPA ($\mu\text{mol kg}^{-1}$) as a function of pH (each point
332 having being acquired after 24 h incubation): as a whole, the overall amount of adsorbed MPCA is
333 maximum below pH 4, decreasing as pH increases. Such a behaviour may be interpreted by
334 considering the ζ -potential curve in Fig. 1d, where the net positive charge of the NTs progressively
335 decreases as pH increases, until the PZC is reached (pH 8.6). In agreement with SAXS data in Fig. 5
336 (*vide infra*), the curve in Fig. 3a seems to point out the fact that the herbicide mainly interacts with
337 the NTs outer surface.

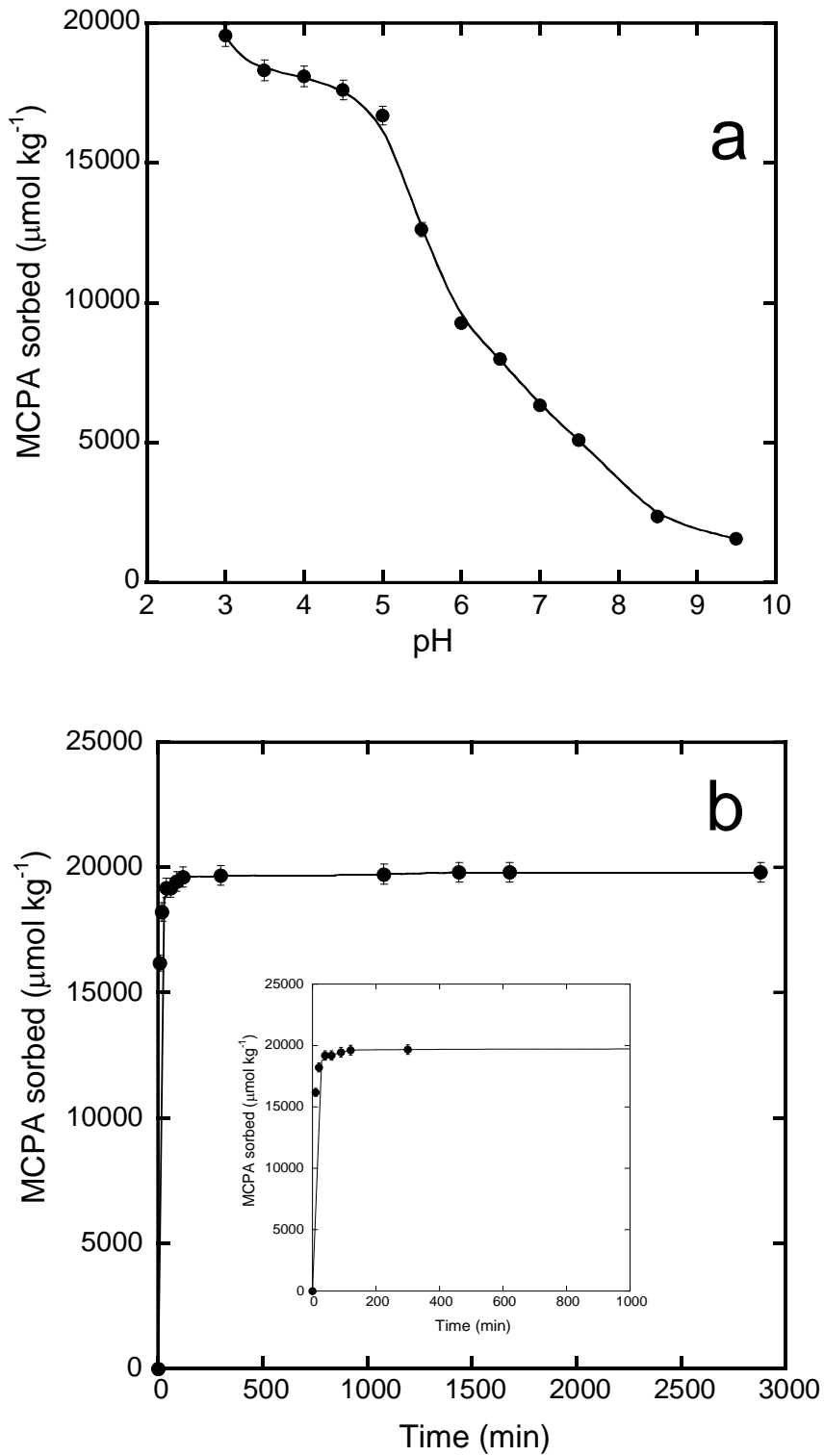
338 Fig. 3b shows the adsorbed amount of MCPA as a function of time at a constant pH of 3.5,
339 i.e. a pH value at which simultaneously the adsorbed amount is very high (Fig. 3a) and the NTs ζ
340 potential is ca. + 37 mV, a condition proper of a stable suspension (Honary and Zahir, 2013). In such
341 condition, aggregation of NTs into bundles should be limited, finally maximizing the available
342 external surface and, thus, MCPA adsorption. The curve in Fig. 3b shows indeed a steep increase in
343 the adsorbed MCPA during the first minutes (inset), reaching complete adsorption after 1440 min. In
344 the adopted experimental conditions (i.e. pH = 3.5 and initial concentration of MCPA = $1.0 \cdot 10^{-5} \text{ M}$),
345 such a phenomenon can be readily assigned to the occurrence of electrostatic interactions. The best

346 model describing the sorption kinetics in Fig. 3b was the pseudo second-order model, which can be
347 expressed in a linear form according to eq. (2) (Ozacar and Sengyl, 2006):

348
$$\frac{t}{q} = \frac{1}{k_2 * q_e^2} - \frac{t}{q_e} \quad (2)$$

349 where q_e and q are the amount of organic pollutant adsorbed ($\mu\text{mol kg}^{-1}$ MCPA) at equilibrium and
350 at time t , respectively, k_2 is the rate constant of adsorption ($\text{kg}/\mu\text{mol h}$) and t is the time (h). For
351 MCPA, the following values were calculated $q_e = 19821.99 \mu\text{mol kg}^{-1}$ and $k_2 = 1.558 \times 10^{-3} \text{ kg}/\mu\text{mol}$
352 h, with an $r^2 = 1$ confirming that the curve-fit procedure was appropriate.

353



354

355 **Figure 3.** Section a: MCPA adsorbed amount as a function of pH (incubation time = 24 h;

356 initial MCPA concentration = $1.0 \cdot 10^{-5}$ M). Section b: MCPA adsorbed amount as a function of time

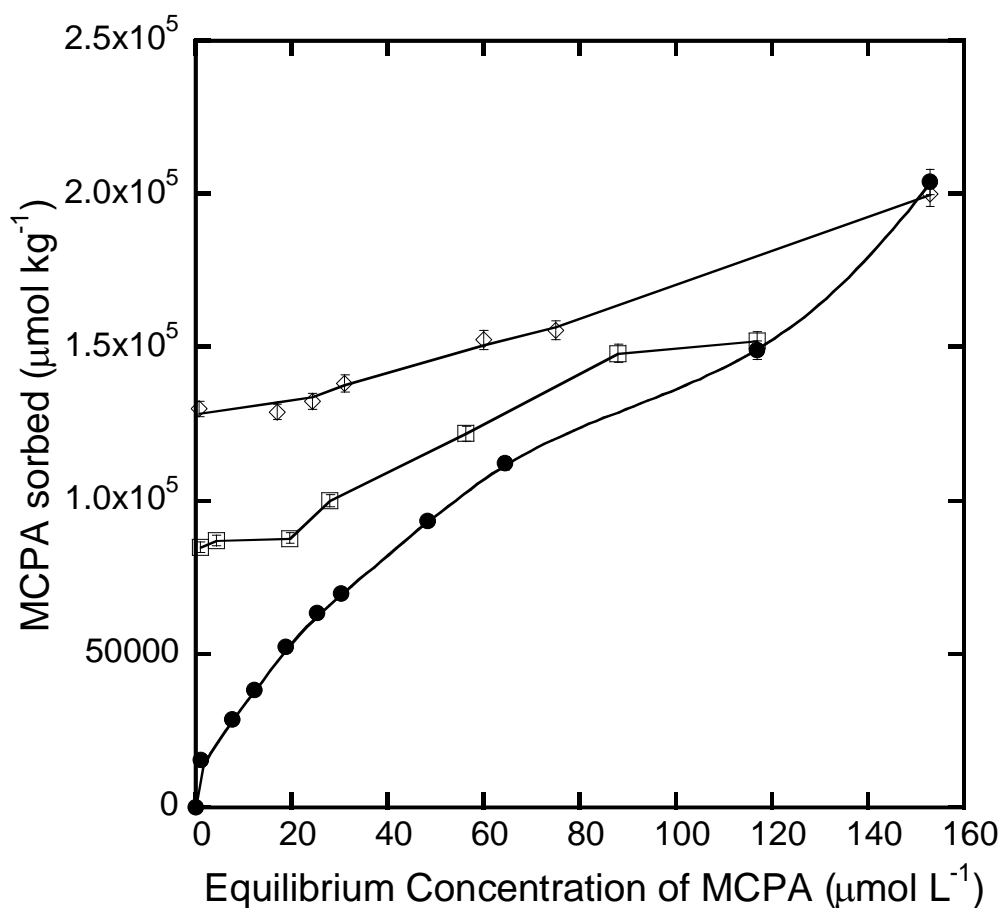
357 at pH = 3.5 (initial MCPA concentration = $1.0 \cdot 10^{-5}$ M). Inset to section b: magnification of the 0-
358 1000 min range.

359 Figure 4 reports MCPA adsorption/desorption equilibrium isotherms at pH = 3.5. The
360 adsorption isotherm (black symbols) has a complex shape, which can be due to multiple phenomena
361 occurring at the NTs outer surface at increasing MCPA concentration. Being the pKa of MCPA in
362 water equal to 2.90 (Addorisio et al., 2010), at pH = 3.5 its dissociation degree (α) is ca. 0.5 and, thus,
363 besides electrostatic interaction, other types of interactions may occur with the outer surface of NTs,
364 like H-bonding, as previously shown by some of us for MCPA adsorption on (mesoporous) Al_2O_3
365 and Fe_2O_3 . (Addorisio et al., 2010) Interestingly, at higher MCPA equilibrium concentration, the
366 adsorption isotherm becomes convex, indicating that the adsorbing species has a lower affinity for
367 the adsorbent: multi-layer adsorption could, indeed, occur, as in MCPA crystals, where multiple inter-
368 molecular bonds form (Kobyłecka et al., 2015).

369 So far, different adsorbents have been investigated for the removal of phenoxy herbicides,
370 including layered double hydroxides (Bruna et al., 2009; Ahmad et al., 2010; Kamaraj et al., 2014),
371 mesoporous metal oxides (Addorisio et al., 2010), resins (Ding et al., 2012) and carbon materials
372 (Kim et al., 2008). In particular, MCPA adsorption was studied on an Argentine montmorillonite
373 (MMT) and its organo-hybrid (OMMT) (Santiago et al., 2016): although adsorption on OMMT (0.05
374 mol/kg) increased with respect to MMT (ca. 0.01 mol/kg), the MCPA adsorbed amounts were
375 significantly lower with respect to that obtained in the adopted experimental conditions with Me-IMO
376 NTs, i.e. ca. 0.2 mol/kg. Such a value is particularly sound if compared to the amount of MCPA
377 adsorbed at pH = 4.0 on a mesoporous alumina with $\text{SSA} = 195 \text{ m}^2 \text{ g}^{-1}$ (0.01 mol/kg), i.e. an adsorbent
378 with similar chemical composition, where diffusion limits occurred (Addorisio et al., 2010).

379 Here, MCPA adsorption likely occurs at the outer surface of the NTs, thus overcoming the
380 aforementioned diffusion limitations during adsorption. However, the two desorption curves (white
381 symbols, Fig. 4) showed that, in the adopted experimental conditions, MCPA adsorption is only
382 partially irreversible, in that the desorbed amount of MCPA was ca. the 35 % and the 44% of the total

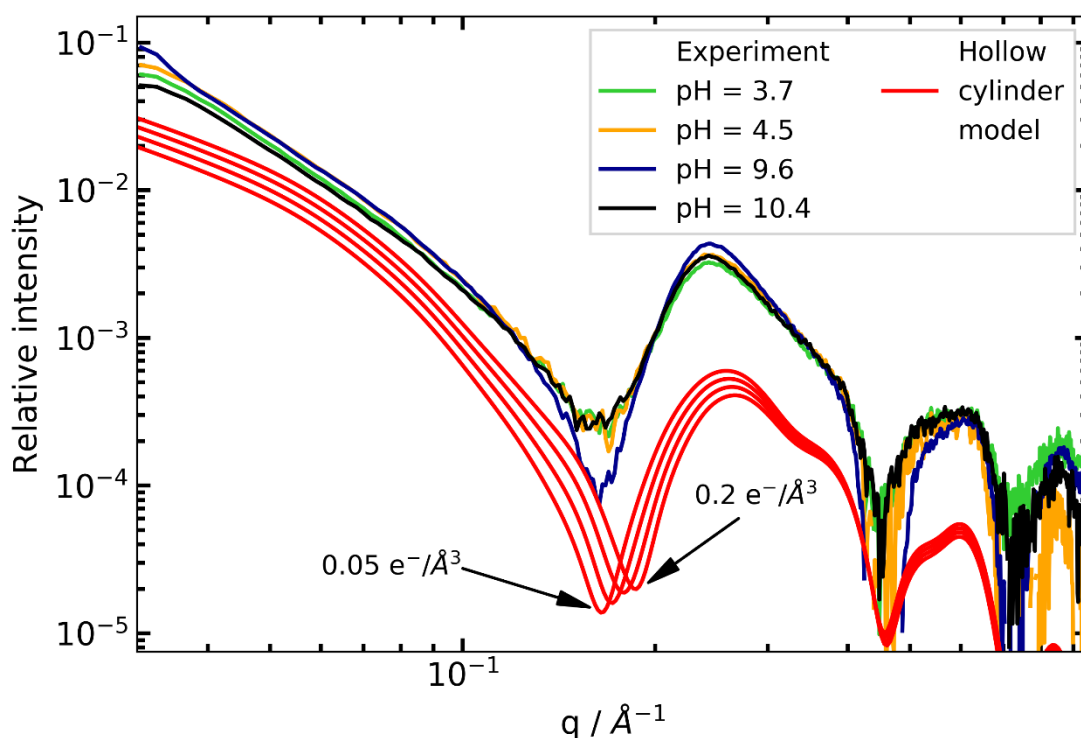
383 amount of adsorbed MCPA (when starting from 129820 $\mu\text{mol/kg}$ and 84790 $\mu\text{mol/kg}$. respectively).
 384 It should be noticed that MCPA adsorption at the outer surface of the NTs is surely perturbing their
 385 actual surface charge, which very likely decreases and, thus, the dispersion could become less stable,
 386 with consequent NTs agglomeration, finally hampering effective desorption of MCPA.



387
 388 **Figure 4.** Adsorption (black circles) isotherm and desorption (white symbols) isotherms of MCPA
 389 on Me-IMO-NTs as obtained at pH = 3.5 in the 0 -160 $\mu\text{mol L}^{-1}$ equilibrium concentration range.

390
 391 In order to confirm the preferential interaction with the outer surface of NTs, Figure 5a reports
 392 the SAXS spectra taken after contacting the Me-IMO NTs with MCPA $1.0 \cdot 10^{-4}$ M in water at pH
 393 3.7, 4.5, 9.6 and 10.4. The bulk electron density of MCPA is $\rho_{\text{MCPA}} = 0.48 \text{ e}^{-}/\text{\AA}^3$. In principle, the
 394 molecular size of MCPA (Table 1) allows adsorption within A pores: if so, a corresponding increase

395 of the NTs inner electronic density should be measured by SAXS (Fig. 5), since the position of the
 396 first minimum of the scattered intensity is very sensitive to changes of the internal scattering length
 397 density. In order to better illustrate this, the scattered intensities of model NTs with internal electronic
 398 density varying from 0.05 to 0.2 $e/\text{\AA}^3$ are plotted in Fig. 5. Interestingly, the position of the first
 399 minimum of the experimental scattered intensity does not shift with pH. Such a constant inner NTs
 400 electronic density allows excluding any interaction of MCPA with the NTs inner surface.



401
 402 **Figure 5.** Experimental SAXS patterns of Me-IMO NTs in MCPA water suspensions at pH =
 403 3.7, 4.5, 9.6 and 10.4 and calculated SAXS patterns (red curves), showing a shift of the scattering
 404 model of hollow cylinder at increasing internal electronic density (from 0.05 to 0.2 $e/\text{\AA}^3$).

405
 406 *3.3. Adsorption of DCM as studied in batch conditions and by SAXS.*

407 Figure 6a reports the pH dependence of DCM adsorbed on Me-IMO NTs: the curve shape is
 408 very different with respect to that concerning MCPA (Fig. 3a), where the adsorbed amount decreases
 409 with pH because, simultaneously, the NTs outer surface becomes less positively charged. With DCM,
 410 adsorption is maximum at pH = 5.5 and, then, decreases.

411 DCM has a non-negligible dipole moment ($\mu = 1.470$ D) and can be polarized by the polar
412 outer NTs walls, leading to dipolar interactions. Simultaneously, its kinetic diameter (0.33 nm) allows
413 DCM diffusion within A pores, but also within B pores having a diameter of 0.45 nm, (Bottero et al.,
414 2011; Bonelli et al., 2013b) and which are able to strongly polarize $\text{CO}_{2(\text{g})}$ molecules in gas-solid
415 systems (Zanzottera et al., 2012a; Bonelli et al., 2013b). Although different phenomena affect
416 adsorption in liquid/solid systems, it is interesting to notice that DCM adsorption is maximum at pH
417 5.5, at which the ζ -potential of the Me-IMO NTs is ca. + 30 mV, likely implying some NTs
418 agglomeration with formation of (more) B pores, where the DCM molecules may diffuse and be
419 polarized, like $\text{CO}_{2(\text{g})}$ molecules (Zanzottera et al., 2012a). Accordingly, the kinetic curve in Fig. 6b
420 has a smooth knee (inset) before reaching a plateau, indicating that more than one type of interaction
421 likely occurs. Application of eq. (2) to model the DCM sorption kinetics in Fig. 6b (Ozacar and
422 Sengyl, 2006) allowed calculating the following parameters: $q_e = 209.04$ mol kg^{-1} and $k_2 = 0.0305$
423 kg/mol h , $r^2 = 0.99$. The extremely high amount of adsorbed DCM could be explained by considering
424 that in oil/water emulsions, such hybrid NTs adsorb at the oil/water interface, stabilizing Pickering
425 emulsions (Picot et al., 2016), modifying the viscosity and, possibly, favouring transport of small
426 molecules within the NTs.

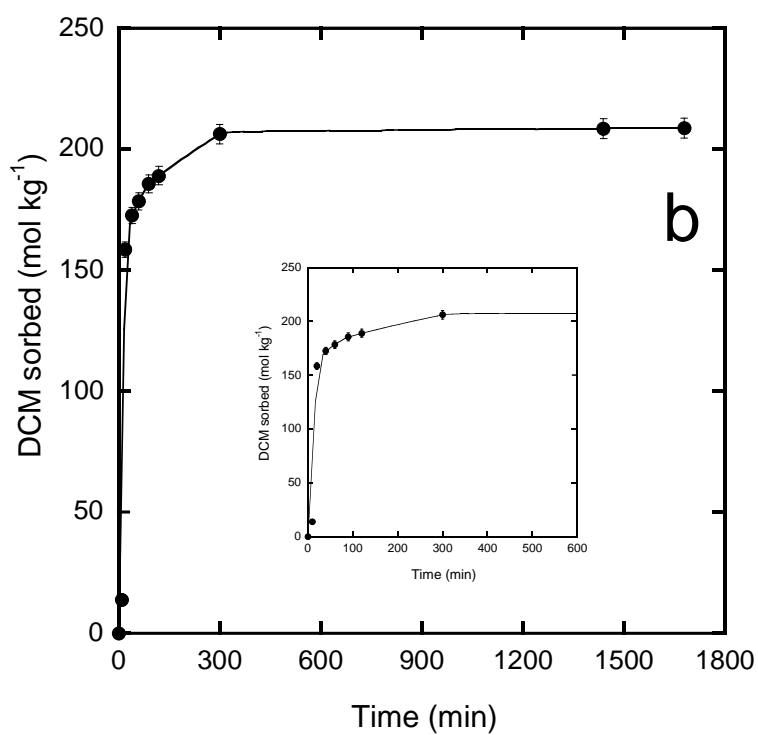
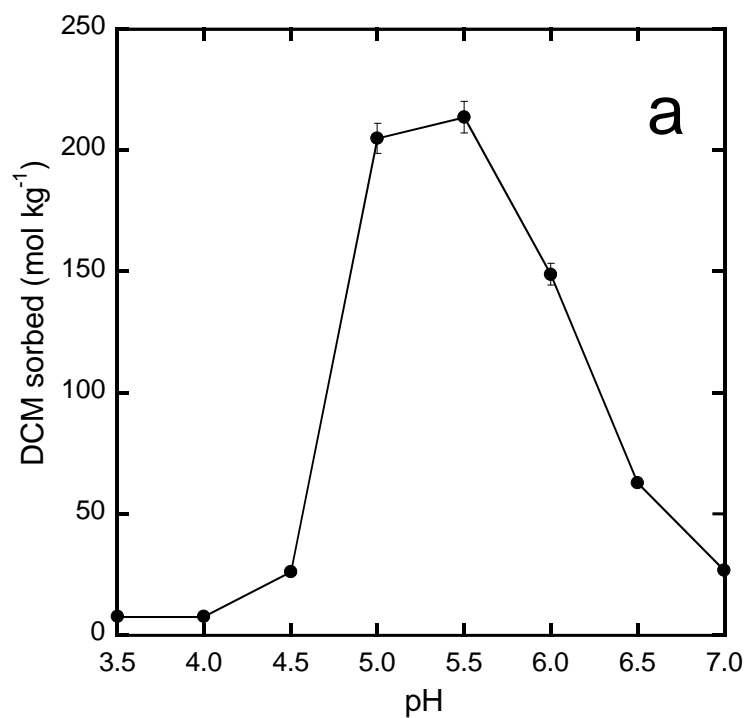
427 Accordingly, the adsorption isotherm in Fig. 7 (black symbols) has an S-shape, indicating that
428 at least two types of adsorption phenomena occur: at low concentration, DCM molecules should
429 interact with stronger adsorbing sites, since their sizeable dipole moment allows interaction with
430 polarizing sites, like B pores, stemming from partial NTs agglomeration into small bundles, and able
431 to polarize DCM molecules (kinetic diameter = 0.33 nm). At increasing pH value, the outer surface
432 of NTs (C surface) becomes less positively charged, thus lowering the adsorption capacity of the
433 outer surface of the NTs towards DCM molecules. Unfortunately, the electronic density of DCM
434 (Table 1) is very close to that of water ($\rho_{\text{H}_2\text{O}} = 0.334$ e $^{-}/\text{\AA}^3$) and, thus, if such a phenomenon should
435 happen, it would be hardly discernible by SAXS, which instead could readily show DCM diffusion
436 within the NTs (A pores, *vide infra*). The latter phenomenon is likely responsible of the largest

437 adsorbed amount of DCM above 0.02 mol/L equilibrium concentration, although in those conditions
438 an oil-in-water Pickering emulsion could form (Picot et al., 2016).

439 As a whole, the thorough understanding of the interaction of DCM with Me-IMO NTs is
440 complicated both by the nature of the pollutant and by formation of Pickering emulsions (Picot et al.,
441 2016).

442 Concerning DCM removal from polluted water, adsorption is considered by the literature as one
443 the most applicable techniques (Lemus et al., 2012; Zhou et al., 2014, 2017), but it requires porous
444 materials with sound adsorbing capacity and high stability. The DCM adsorption capacity of Zr-based
445 metal-organic framework (UiO-66) was enhanced in the presence of UiO-66 crystals with various
446 morphologies and optimized porous structure as obtained by adjusting the synthesis procedure. (Zhou
447 et al., 2017): however, in the adopted experimental conditions, the maximum adsorption capacity was
448 lower than here (ca. 6 mmol/kg).

449 As for MCPA, in the adopted experimental conditions DCM desorption was not fully
450 reversible (white symbols in Fig. 7) indicating the likely occurrence of mass transfer phenomena,
451 related to some NTs aggregation, which hampers DCM molecules diffusion of DCM from the interior
452 of the NTs/bundles to the exterior. However, such diffusion limitations, occurring especially during
453 desorption, could be overcome by changing operative conditions, e.g. liquid/solid ratio, and require
454 dedicated studies.



455

456

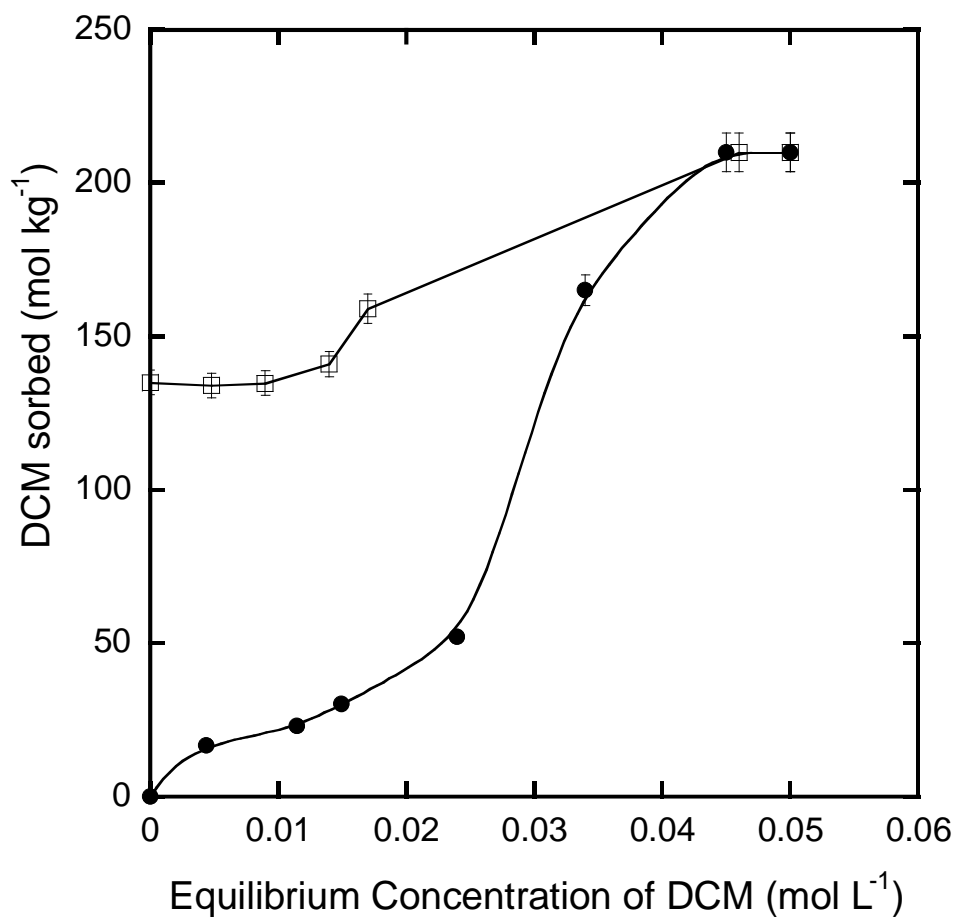
457

458

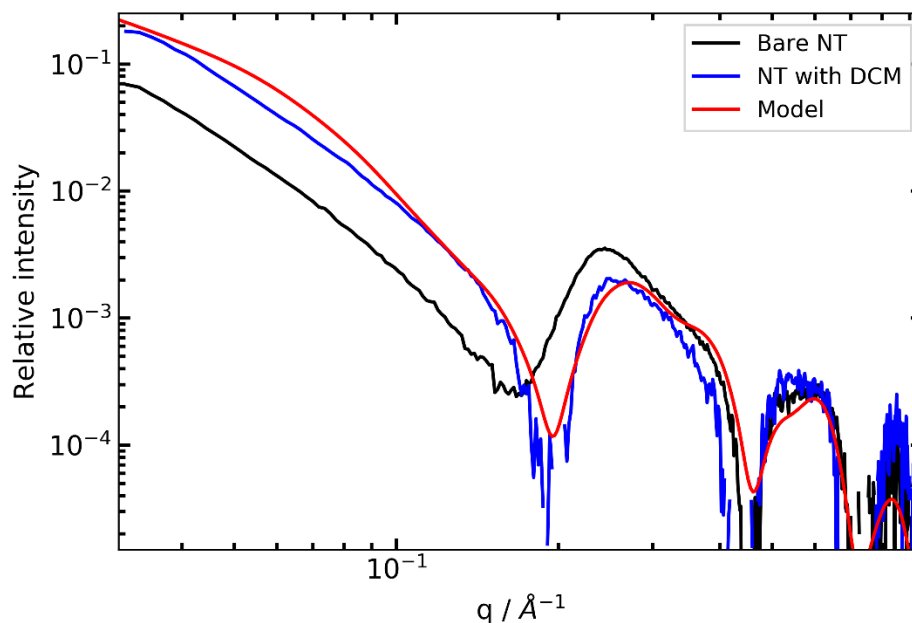
Figure 6. Section a: DCM adsorbed amount as a function of pH. Incubation time: 24 h. Initial

DCM concentration: 0.15 M. Section b: DCM adsorbed amount as a function of time, pH = 5.5; initial

459 DCM concentration: 0.15 M. Inset to section b: magnification of the 0-600 min range, where the
460 maximum amount of adsorbed DCM is reached after 300 min.
461



462
463
464 **Figure 7.** Adsorption (black symbols) isotherm and desorption isotherm (white symbols) of DCM on
465 Me-IMO-NTs at pH = 5.5 in the 0 -0.06 mol L⁻¹ equilibrium concentration range.
466



467

468 **Figure 8.** SAXS patterns of Me-IMO NTs in the DCM suspension at natural pH. The scattering model
 469 for a hollow cylinder show the variation of internal electronic density from 0.05 to 0.29 $e/\text{\AA}^3$.

470

471 Fig. 8 reports the SAXS patterns observed when the NTs are contacted with DCM suspension.
 472 The position of the first minimum shifts towards higher q values, indicating an increase of the inner
 473 electronic density. The applied model yields a value of ρ_i equal to 0.29 $e/\text{\AA}^3$ for the inner electron
 474 density of Me-IMO NTs, proving that DCM (bulk DCM has $\rho = 0.4 e/\text{\AA}^3$, Table 1) has indeed entered
 475 the NTs. The high adsorbed amounts measured by batch experiments indicate that the DCM
 476 molecules adsorb also at the outer surface of NTs and not only within them, but since the SAXS
 477 measurement is based on a change on the internal electron density, it may be unable to detected the
 478 change in the outer electron density, since the NTs are suspended in water, which has a high electron
 479 density.

480

481 Conclusions

482 Methylmogolite NTs have two types of surface, namely an inner one, which is extremely
 483 hydrophobic, and an outer one, which is hydrophilic, polar and positively charged below pH 8.6. The

484 external positive charge affects the NTs behaviour in water: for instance, by varying pH, NTs
485 arrangement changes, likely leading to some aggregation phenomena that, in turn, affect both
486 adsorption and desorption processes in water.

487 Adsorption of two organic pollutants (namely MCPA, 2-methyl-4-chlorophenoxyacetic acid,
488 and DCM, dichloromethane) on methylimogolite occurs through complex interactions, which can be
489 only partially explained by the joint use of batch experiments and SAXS measurements.

490 On the one hand, the reported results show that MCPA adsorption occurs at the outer surface
491 of the NTs by means of both electrostatic interactions and intermolecular forces, with sound overall
492 adsorbed amounts as compared to another mesoporous adsorbent (i.e. Al_2O_3) with a chemical
493 composition similar to that of the NTs outer surface.

494 On the other hand, unravelling the type of interaction of DCM with methylimogolite is not
495 straightforward. SAXS measurements clearly showed diffusion of DCM molecules within A pores
496 and batch experiments showed high adsorbed amounts. However, the latter type of measurements
497 seem to point out the interaction with another type of surface, most likely B pores forming among
498 three aligned NTs in a bundle: unfortunately, this type of interaction that cannot be clearly assessed
499 by SAXS. Moreover, on the basis of previous studies, stabilization of an emulsion induced by the
500 same NTs could not be excluded.

501 To the best of our knowledge, this is the first work assessing the adsorption/desorption of
502 organic molecules of environmental concern with this type of nanomaterial and could open new
503 perspectives for its practical application, undoubtedly after optimization of the desorption process,
504 which requires dedicated studies.

505

506 **Acknowledgements**

507 Financial support from Università Italo-Francese (Galileo Project Grant n°G16 – 34 «Hybrid
508 imogolite nanotubes for environmental applications») is acknowledged.

509

510 **References**

511 Ackerman, W.C., Smith, D.M., Huling, J.C., Kim, Y.W., Bailey, J.K., Brinker, C.J., 1993.

512 Gas/Vapor Adsorption in Imogolite: A Microporous Tubular Aluminosilicate. *Langmuir* 9,
513 1051–1057. <https://doi.org/10.1021/la00028a029>

514 Addorisio, V., Esposito, S., Sannino, F., 2010. Sorption Capacity of Mesoporous Metal Oxides for
515 the Removal of MCPA from Polluted Waters. *J. Agric. Food Chem.* 58, 5011–5016.

516 <https://doi.org/10.1021/jf9044815>

517 Ahmad, T., Rafatullah, M., Ghazali, A., Sulaiman, O., Hashim, R., Ahmad, A., 2010. Removal of
518 pesticides from water and wastewater by different adsorbents: A review. *J. Environ. Sci. Heal.*
519 - Part C Environ. Carcinog. Ecotoxicol. Rev. 28, 231–271.

520 <https://doi.org/10.1080/10590501.2010.525782>

521 Amara, M.S., Paineau, E., Tache, O., Launois, P., Thill, A., 2015. Hybrid , Tunable-Diameter ,
522 Metal Oxide Nanotubes for Trapping of Organic Molecules.

523 <https://doi.org/10.1021/cm503428q>

524 Bahadori, E., Vaiano, V., Esposito, S., Armandi, M., Sannino, D., Bonelli, B., 2018. Photo-
525 activated degradation of tartrazine by H₂O₂ as catalyzed by both bare and Fe-doped methyl-
526 imogolite nanotubes. *Catal. Today* 304, 199–207. <https://doi.org/10.1016/j.cattod.2017.08.003>

527 Bonelli, B., 2016. Surface Chemical Modifications of Imogolite, in: Yuan, P., Thill, A., Bergaya, F.
528 (Eds.), *Developments in Clay Science*. Elsevier B.V, pp. 279–307.

529 <https://doi.org/10.1016/B978-0-08-100293-3.00012-1>

- 530 Bonelli, B., Armandi, M., Garrone, E., 2013a. Surface properties of alumino-silicate single-walled
531 nanotubes of the imogolite type. *Phys. Chem. Chem. Phys.* 15, 13381–13390.
532 <https://doi.org/10.1039/c3cp51508g>
- 533 Bonelli, B., Bottero, I., Ballarini, N., Passeri, S., Cavani, F., Garrone, E., 2009. IR spectroscopic
534 and catalytic characterization of the acidity of imogolite-based systems. *J. Catal.* 264, 15–30.
535 <https://doi.org/10.1016/j.jcat.2009.03.003>
- 536 Bonelli, B., Zanzottera, C., Armandi, M., Esposito, S., Garrone, E., 2013b. IR spectroscopic study
537 of the acidic properties of alumino-silicate single-walled nanotubes of the imogolite type.
538 *Catal. Today* 218–219, 3–9. <https://doi.org/10.1016/j.cattod.2013.02.004>
- 539 Bottero, I., Bonelli, B., Ashbrook, S.E., Wright, P.A., Zhou, W., Tagliabue, M., Armandi, M.,
540 Garrone, E., 2011. Synthesis and characterization of hybrid organic/inorganic nanotubes of the
541 imogolite type and their behaviour towards methane adsorption. *Phys. Chem. Chem. Phys.* 13,
542 744–750. <https://doi.org/10.1039/c0cp00438c>
- 543 Boyer, M., Paineau, E., Bacia-verloop, M., Thill, A., 2014. Applied Clay Science Aqueous
544 dispersion state of amphiphilic hybrid aluminosilicate nanotubes. *Appl. Clay Sci.* 96, 45–49.
545 <https://doi.org/10.1016/j.clay.2014.04.022>
- 546 Bruna, F., Celis, R., Pavlovic, I., Barriga, C., Cornejo, J., Ulibarri, M.A., 2009. Layered double
547 hydroxides as adsorbents and carriers of the herbicide (4-chloro-2-methylphenoxy)acetic acid
548 (MCPA): Systems Mg-Al, Mg-Fe and Mg-Al-Fe. *J. Hazard. Mater.* 168, 1476–1481.
549 <https://doi.org/10.1016/j.jhazmat.2009.03.038>
- 550 Bursill, L.A., Peng, J.L., Bourgeois, L.N., 2000. Imogolite : An aluminosilicate nanotube material.
551 *Philos. Mag. A* 80, 105–117. <https://doi.org/10.1080/01418610008212043>
- 552 Cradwick, P.D.G., Farmer, V.C., Russell, J.D., Masson, C.R., Wada, K., Yoshinaga, N., 1972.

553 Imogolite, a Hydrated Aluminium Silicate of Tubular Structure. *Nat. Phys. Sci.* 240, 187–189.
554 <https://doi.org/10.1038/physci240187a0>

555 Ding, L., Lu, X., Deng, H., Zhang, X., 2012. Adsorptive removal of 2,4-dichlorophenoxyacetic acid
556 (2,4-D) from aqueous solutions using MIEX resin. *Ind. Eng. Chem. Res.* 51, 11226–11235.
557 <https://doi.org/10.1021/ie300469h>

558 Du, P., Yuan, P., Thill, A., Annabi-Bergaya, F., Liu, D., Wang, S., 2017. Insights into the formation
559 mechanism of imogolite from a full-range observation of its sol-gel growth. *Appl. Clay Sci.*
560 150, 115–124. <https://doi.org/10.1016/j.clay.2017.09.021>

561 Freyria, F.S., Geobaldo, F., Bonelli, B., 2018. Nanomaterials for the abatement of pharmaceuticals
562 and personal care products from wastewater. *Appl. Sci.* 8, 170.
563 <https://doi.org/10.3390/app8020170>

564 Garrone, E., Bonelli, B., 2016. Imogolite for Catalysis and Adsorption, in: Yuan, P., Thill, A.,
565 Bergaya, F. (Eds.), *Developments in Clay Science*. Elsevier B.V, pp. 672–707.
566 <https://doi.org/10.1016/B978-0-08-100293-3.00025-X>

567 Gimeno, O., Plucinski, P., Kolaczowski, S.T., Rivas, F.J., Alvarez, P.M., 2003. Removal of the
568 Herbicide MCPA by Commercial Activated Carbons : Equilibrium , Kinetics , and
569 Reversibility 22, 1076–1086. <https://doi.org/10.1021/ie020424x>

570 Gustafsson, J.P., 2001. The surface chemistry of imogolite. *Clays Clay Miner.* 49, 73–80.

571 Honary, S., Zahir, F., 2013. Effect of Zeta Potential on the Properties of Nano-Drug Delivery
572 Systems - A Review (Part 2) 12, 265–273.

573 Huang, B., Lei, C., Wei, C., Zeng, G., 2014. Chlorinated volatile organic compounds (Cl-VOCs)
574 in environment — sources , potential human health impacts , and current remediation
575 technologies. *Environ. Int.* 71, 118–138. <https://doi.org/10.1016/j.envint.2014.06.013>

576 Kamaraj, R., Davidson, D.J., Sozhan, G., Vasudevan, S., 2014. An in situ electrosynthesis of metal
577 hydroxides and their application for adsorption of 4-chloro-2-methylphenoxyacetic acid
578 (MCPA) from aqueous solution. *J. Environ. Chem. Eng.* 2, 2068–2077.
579 <https://doi.org/10.1016/j.jece.2014.08.027>

580 Karube, J., 1998. Notes: Hysteris of the colloidal stability of imogolite. *Clays Clay Miner.* 583–584.
581 <https://doi.org/10.1346/CCMN.1998.0460512>

582 Kim, T.Y., Park, S.S., Kim, S.J., Cho, S.Y., 2008. Separation characteristics of some phenoxy
583 herbicides from aqueous solution. *Adsorption* 14, 611–619. [https://doi.org/10.1007/s10450-](https://doi.org/10.1007/s10450-008-9129-6)
584 [008-9129-6](https://doi.org/10.1007/s10450-008-9129-6)

585 Kobylecka, J., Turek, A., Siero, L., 2015. Crystal Packing and Supramolecular Motifs in Four
586 Phenoxyalkanoic Acid Crystal Packing and Supramolecular Motifs in Four Phenoxyalkanoic
587 Acid Herbicides — Low-Temperature Redeterminations. *Org. Chem. Int.* ID 608165.
588 <https://doi.org/10.1155/2011/608165>

589 Lemus, J., Martin-Martinez, M., Palomar, J., Gomez-Sainero, L., Gilarranz, M.A., Rodriguez, J.J.,
590 2012. Removal of chlorinated organic volatile compounds by gas phase adsorption with
591 activated carbon. *Chem. Eng. J.* 211–212, 246–254. <https://doi.org/10.1016/j.cej.2012.09.021>

592 Mackenzie, K.J.D., 1989. Structure and Thermal Transformations of Imogolite Studied by ²⁹Si and
593 ²⁷Al High-Resolution Solid-State Nuclear Magnetic Resonance. *Clays Clay Miner.* 37, 317–
594 324. <https://doi.org/10.1346/CCMN.1989.0370404>

595 Mizota, C., 1977. Phosphate fixation by ando soils different in their clay mineral composition. *Soil*
596 *Sci. Plant Nutr.* 23, 311–318. <https://doi.org/10.1080/00380768.1977.10433050>

597 Ozacar, M., Sengyl, I., 2006. A two stage batch adsorber design for methylene blue removal to
598 minimize contact time. *J. Environ. Manag.* 80, 372–379.

599 <https://doi.org/10.1016/j.jenvman.2005.10.004>

600 Parfitt, R.L., 2009. Allophane and imogolite : role in soil biogeochemical processes. *Clay Miner.*
601 44, 135–155. <https://doi.org/10.1180/claymin.2009.044.1.135>

602 Picot, P., Gobeaux, F., Coradin, T., Thill, A., 2019. Dual internal functionalization of imogolite
603 nanotubes as evidenced by optical properties of Nile red. *Appl. Clay Sci.* 178, 1015133.
604 <https://doi.org/10.1016/j.clay.2019.105133>

605 Picot, P., Malloggi, F., Coradin, T., Thill, A., 2016. Behaviour of hybrid inside/out Janus nanotubes
606 at an oil/water interface. A route to self-assembled nanofluidics? *Faraday Discuss.* 191, 1–5.
607 <https://doi.org/10.1039/C6FD00034G>

608 Poli, E., Elliott, J.D., Hine, N.D.M., Mostofi, A.A., Teobaldi, G., Elliott, J.D., Hine, N.D.M.,
609 Mostofi, A.A., Teobaldi, G., Poli, E., Elliott, J.D., Hine, N.D.M., Mostofi, A.A., Teobaldi, G.,
610 2015. Large-scale density functional theory simulation of inorganic nanotubes : a case study on
611 Imogolite nanotubes 19, S272. <https://doi.org/10.1179/1432891715Z.0000000001560>

612 Rojas-Mancilla, E., Oyarce, A., Alvarado-soto, L., Ram, R., 2019. Imogolite Synthetized in
613 Presence of As(III) Induces Low Cell Toxicity and Hemolysis , in Vitro , Potential
614 Stabilization of Arsenite Present in Aqueous Systems 4, 10510–10515.
615 <https://doi.org/10.1021/acsomega.8b03357>

616 Santiago, C.C., Fernández, M.A., Torres Sánchez, R.M., 2016. Adsorption and characterization of
617 MCPA on DDTMA- and raw-montmorillonite: Surface sites involved. *J. Environ. Sci. Heal. -*
618 *Part B Pestic. Food Contam. Agric. Wastes* 51, 245–253.
619 <https://doi.org/10.1080/03601234.2015.1120618>

620 Shafia, E., Esposito, S., Armandi, M., Bahadori, E., Garrone, E., Bonelli, B., 2016a. Reactivity of
621 bare and Fe-doped alumino-silicate nanotubes (imogolite) with H₂O₂ and the azo-dye Acid

622 Orange 7. *Catal. Today* 277, 89–96. <https://doi.org/10.1016/j.cattod.2015.10.011>

623 Shafia, E., Esposito, S., Bahadori, E., Armandi, M., Manzoli, M., Bonelli, B., 2016b. Synthesis and
624 characterization of Fe-doped aluminosilicate nanotubes with enhanced electron conductive
625 properties. *J. Vis. Exp.* 117, e54758. <https://doi.org/10.3791/54758>

626 Thill, A., Picot, P., Belloni, L., 2017. A mechanism for the sphere/tube shape transition of
627 nanoparticles with an imogolite local structure (imogolite and allophane). *Appl. Clay Sci.* 141,
628 308–315. <https://doi.org/10.1016/j.clay.2017.03.011>

629 Zanzottera, C., Armandi, M., Esposito, S., Garrone, E., Bonelli, B., 2012a. CO₂ adsorption on
630 aluminosilicate single-walled nanotubes of imogolite type. *J. Phys. Chem. C* 116, 20417–
631 20425. <https://doi.org/10.1021/jp3061637>

632 Zanzottera, C., Vicente, A., Armandi, M., Fernandez, C., Garrone, E., Bonelli, B., 2012b. Thermal
633 collapse of single-walled alumino-silicate nanotubes: Transformation mechanisms and
634 morphology of the resulting lamellar phases. *J. Phys. Chem. C* 116, 23577–23584.
635 <https://doi.org/10.1021/jp3090638>

636 Zhou, L., Chen, Y.L., Zhang, X.H., Tian, F.M., Zu, Z.N., 2014. Zeolites developed from mixed
637 alkali modified coal fly ash for adsorption of volatile organic compounds. *Mater. Lett.* 119,
638 140–142. <https://doi.org/10.1016/j.matlet.2013.12.097>

639 Zhou, L., Zhang, X., Chen, Y., 2017. Modulated synthesis of zirconium metal–organic framework
640 UiO-66 with enhanced dichloromethane adsorption capacity. *Mater. Lett.* 197, 167–170.
641 <https://doi.org/10.1016/j.matlet.2017.03.162>

642

643